Available online at www.sciencedirect.com
SCIENCE DIRECT®
Earth and Planetary Science Letters 242 (2006) 39–50
EPSL
www.elsevier.com/locate/epsl

Sclerite formation in the hydrothermal-vent "scaly-foot" gastropod—possible control of iron sulfide biomineralization by the animal

Yohey Suzuki [a,*], Robert E. Kopp [b], Toshihiro Kogure [c], Akinobu Suga [d], Ken Takai [a], Shinji Tsuchida [e], Noriaki Ozaki [f], Kazuyoshi Endo [g], Jun Hashimoto [h], Yasuhiro Kato [i], Chitoshi Mizota [j], Takafumi Hirata [d], Hitoshi Chiba [k], Kenneth H. Nealson [a,l], Koki Horikoshi [a], Joseph L. Kirschvink [b]

[a] *Extremobiosphere Research Center, Japan Agency for Marine-Earth Science & Technology, Yokosuka 237-0061, Japan*
[b] *Division of Geological and Planetary Sciences, California Institute of Technology, Pasadena, CA 91125, USA*
[c] *Department of Earth and Planetary Science, the University of Tokyo, Hongo, Tokyo 113-0033, Japan*
[d] *Laboratory for Planetary Sciences, Tokyo Institute of Technology, Meguro, Tokyo 152-8551, Japan*
[e] *Marine Ecosystems Research Department, Japan Agency for Marine-Earth Science & Technology, Yokosuka 237-0061, Japan*
[f] *Ocean Research Institute, University of Tokyo, Nakano, Tokyo 164-8639, Japan*
[g] *Institute of Geoscience, University of Tsukuba, Tsukuba 305-8572, Japan*
[h] *Faculty of Fisheries, Nagasaki University, Nagasaki, 852-8521, Japan*
[i] *Department of Geosystem Engineering, Unversity of Tokyo, Tokyo 113-8656, Japan*
[j] *Faculty of Agriculture, Iwate University, Morioka, Iwate 020-8550, Japan*
[k] *Department of Earth Sciences, Okayama University, Okayama, Okayama 700-8530, Japan*
[l] *Department of Earth Sciences, University of Southern California, 3651 Trousdale Pkwy., Los Angeles, CA 90089-0740, USA*

Received 24 March 2005; received in revised form 23 August 2005; accepted 22 November 2005
Available online 10 January 2006
Editor: E. Boyle

Abstract

A gastropod from a deep-sea hydrothermal field at the Rodriguez triple junction, Indian Ocean, has scale-shaped structures, called sclerites, mineralized with iron sulfides on its foot. No other organisms are known to produce a skeleton consisting of iron sulfides. To investigate whether iron sulfide mineralization is mediated by the gastropod for the function of the sclerites, we performed a detailed physical and chemical characterization. Nanostructural characterization of the iron sulfide sclerites reveals that the iron sulfide minerals pyrite (FeS_2) and greigite (Fe_3S_4) form with unique crystal habits inside and outside of the organic matrix, respectively. The magnetic properties of the sclerites, which are mostly consistent with those predicted from their nanostructual features, are not optimized for magnetoreception and instead support use of the magnetic minerals as structural elements. The mechanical performance of the sclerites is superior to that of other biominerals used in the vent environment for predation as well as protection from predation. These characteristics, as well as the co-occurrence of brachyuran crabs, support the inference that the mineralization of iron sulfides might be controlled by the gastropod to harden the sclerites for protection from predators. Sulfur and iron isotopic analyses indicate that sulfur and iron in the sclerites originate from hydrothermal fluids rather than from bacterial

* Corresponding author. Tel.: +81 46 867 9710; fax: +81 46 867 9715.
E-mail address: yohey@jamstec.go.jp (Y. Suzuki).

0012-821X/$ - see front matter
doi:10.1016/j.epsl.2005.11.029

metabolites, and that iron supply is unlikely to be regulated by the gastropod for iron sulfide mineralization. We propose that the gastropod may control iron sulfide mineralization by modulating the internal concentrations of reduced sulfur compounds.

Keywords: iron sulfides; biomineralization; hydrothermal-vent gastropod; sclerite

1. Introduction

The "scaly-foot" gastropod (Fig. 1), so named for the unusual scale-shaped sclerites on its foot, was discovered recently in the Kairei deep-sea hydrothermal field of the Central Indian Ridge [1]. Black deposits localized in the sclerites are iron sulfide minerals within a laminated organic matrix [1]. Although iron sulfide mineralization is known largely as a byproduct of metabolic sulfate reduction from prokaryotes [2], only a few known species of magnetotactic bacteria that employ greigite magnetosomes are known to control mineralization of iron sulfides [3,4].

Since the advent of animal skeletons, calcium carbonates (mostly calcite, magnesian calcites and aragonite), phosphates (mostly apatite, particularly dahllite, $Ca_5(PO_4,CO_3)_3(OH)$), and opal (a hydrated gel of silica, SiO_2) have been the most common skeleton-forming minerals [5]. The term "sclerite" refers to an element of a composite exoskeleton, one in which the elements are held together to form a protective coating like a coat of mail. In common usage, the term sclerite excludes vertebrate bones, echinoderm ossicles, and sponge spicules, which are all formed endoskeletally, and simple one- or two-part skeletons like gastropod or brachiopod shells (personal communication with S. Bengtson). Sclerites generally compose a modular scleritome with scale- or spine-shaped elements, which is characteristic of numerous Cambrian metazoans (halkieriids, sphogonuchitids, chancelloriids, tommotiids, tannuolinids, cambroclaves, and others) [6,7]. Scleritomes are a less conspicuous feature of modern animals, but they do occur in primitive living mollusks, specifically aplacophorans and polyplacophorans [8]. Whereas scleritomes in these molluscs are composed of calcium-bearing minerals [8], the unique scleritome of the "scaly-foot" gastropod is composed of greigite (Fe_3S_4) and pyrite (FeS_2) [1].

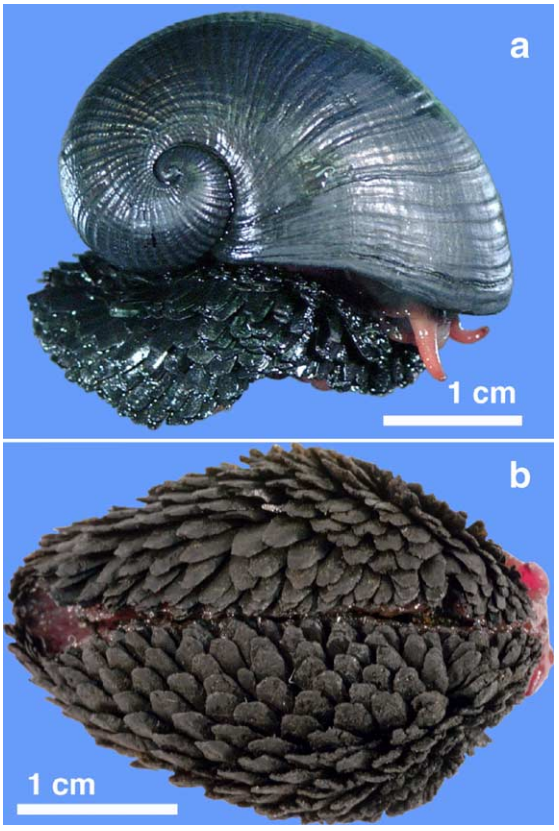

Fig. 1. Structures of the "scaly-foot" gastropod and its foot. (a) Photograph of the "scaly-foot" gastropod from the Kairei field, Indian Ocean. (b) Photograph of scale-shaped sclerites attached to the foot of the gastropod.

It is also rare for animals to produce macroscopic materials that stick to a hand magnet. For many years, the only such structures known were the radular teeth of the *Polyplacophoran* mollusks, the chitons [9], which are hardened by a capping layer of nanometer-sized crystals of the ferromagnetic mineral magnetite (Fe_3O_4) [10]. Subsequent investigations have found that microscopic magnetite-based systems for detecting the Earth's magnetic field occur in diverse organisms, among them magnetotactic bacteria and protists, and virtually all animals (see Kirschvink, J.L., Walker, M.M., Diebel, C.E. Magnetite-based Magnetoreception. Current Opinion in Neurobiology, 11, 462–467, 2001). The magnetization of the scaly-foot gastropod sclerites, like that of chiton teeth, is readily observable and is likely due to greigite, which is strongly ferrimagnetic [1]. One question this discovery raises is whether the iron sulfides in the sclerite, like magnetite in chiton teeth, serves solely as structural elements or whether, like most other occurrences of biogenic magnetic minerals, the iron sulfides also serve as a magnetic sensor.

To investigate the mechanisms by which the iron sulfide minerals form in the sclerites and the possible

function of the iron sulfide scleritome, we characterized the sclerites' nanostructure, magnetic and mechanical properties and sulfur and iron isotopic compositions.

2. Materials and methods

2.1. Sampling

The crewed submersible *Shinkai 6500* collected the "scaly-foot" gastropod from the base of active black smoker chimney structures (25°19.22′S, 70°02.44′E) at a depth of ~2420 m in the Kairei field, Indian Ocean (JAMSTEC Scientific Cruise YK01-15).

2.2. Electron microscopy

Sclerites from three individuals were freeze-dried and embedded in epoxy. The polished surface was observed by SEM by using a Hitachi S4500 and JEOL JSM-6700F equipped with EDS at a 15-kV accelerating voltage. For transmission electron microscopy (TEM), untreated sclerites were thinned by using a focused ion beam (FIB) system on a micro sampling device (Hitachi FB-2000A) at a 30-kV accelerating voltage, and coated with carbon and tungsten. The TEM specimen was observed by the Tecnai G2 F20S-Twin field emission TEM (FEI Inc.) equipped with a Gatan imaging filter (GIF) set to zero-loss filtering with 20-eV energy window. The HF2000 field-emission TEM (Hitachi Inc.) was also used. Both TEMs were equipped with EDS and operated at an accelerating voltage of 200 kV.

2.3. Magnetic studies

Low-temperature magnetic properties of the sclerites were measured using a Quantum Design SQUID Magnetic Properties Measurement System (MPMS). Samples were cooled to 2 K in zero magnetic field, pulsed with a saturating magnetic field of 3 T, and then warmed to 300 K in either zero field or a 5 mT field. Room-temperature hysteresis properties and thermal alteration behavior were measured using a Princeton Measurements MicroMag Vibrating Sample Magnetometer (VSM).

Room temperature remanence magnetizations were measured using a 2G SQUID magnetometer. Anhysteritic remanence magnetization (ARM) was imparted by applying an axial alternating field of 100 mT and a parallel dc biasing field of 0–2 mT. Isothermal remanence magnetization (IRM) was imparted by pulsing the sample with axial fields of up to 300 mT. Rotational remanence magnetization was imparted by spinning the sample at between 2 and 20 Hz while applying a transverse alternating field of 100 mT.

Ferromagnetic resonance spectra were acquired with a Bruker ESP 300E EPR spectrometer as described in Weiss et al. [11].

2.4. Nanoidentation

The mechanical properties of the sclerites were measured with a TriboIndenter indentation instrument (Hysitron Inc.). This TriboIndenter has load and displacement resolutions of 100 nN and 0.2 nm, respectively. Load–penetration depth curves were obtained by indentation measurement. From these curves, the hardness and elastic modulus of the sclerites were determined with the Oliver method [12]. For indentation measurements, the sclerites were embedded in epoxy resin and the surfaces were mechanically polished by using the FIB system (FEI Dual Beam FIB Strata 235) at a 30-kV accelerating voltage.

2.5. Sulfur isotopic analysis

Sclerites were rinsed with deionized water and then decomposed and oxidized by the mixture of Br_2+HNO_3. The resultant sulfate ion was precipitated as $BaSO_4$. The soft body samples were finely sliced and repeatedly washed with 0.1 M LiCl solution to eliminate excess seawater sulfate. After drying, the soft body samples were burned by the Parr Bomb(TM) method. The resultant sulfate ion was converted to $BaSO_4$. $BaSO_4$ was converted to sulfur dioxide by the method of [13] for sulfur isotope analysis. Sulfur isotope ratios were measured with a VG SIRA stable isotope ratio mass-spectrometer. The measured isotopic composition was expressed as $\delta^{34}S$, which can be defined as:

$$\delta^{34}S = [\left(^{34}S/^{32}S\right)_{\text{sample}}/\left(^{34}S/^{32}S\right)_{\text{standard}} - 1]\times 10^3 \quad (1)$$

where $(^{34}S/^{32}S)_{sample}$ is the $^{34}S/^{32}S$ abundance ratio for a sample and $(^{34}S/^{32}S)_{standard}$ is the $^{34}S/^{32}S$ abundance ratio for the Cañon Diablo Troilite (CDT) standard. Values of $\delta^{34}S$ therefore represent differences, in parts per thousand (per mil, ‰), between the $^{34}S/^{32}S$ value of a sample and that of the standard. Typical analytical precision on $\delta^{34}S$ measurement was better than 0.3‰.

2.6. Iron isotopic analysis

About 1 mg of sclerite samples and 0.2–0.5 g of sulfide chimney samples were decomposed by a mix-

ture of 6 M HCl and 7 M HNO_3. For the soft body samples of the gastropods (0.6–1.0 g wet weight), the acid decomposition was preceded by incineration. Iron was collected from the dissolved sample solution by means of anion-exchange chromatography using AG MP-1 (100–200 mesh). Recovery of Fe through the chemical decomposition and separation procedures was >97%. The Fe isotopic ratios were analyzed by a MC-ICP-MS technique (Nu Plasma 500, Wrexham, UK) equipped with a desolvating sample introduction system to minimize the contribution of mass spectrometric interference by $^{56}ArO^{+}$ onto the $^{56}Fe^{+}$ signal. The mass bias factor was externally corrected by a standard-sample-standard bracketing method using IRMM-014. Typical analytical precisions on measurements for $\delta^{56}Fe$ ($^{56}Fe/^{54}Fe$ ratio in per mil, ‰) were better than 0.2‰.

3. Results and discussion

3.1. Behavioral observations

As they do on the deep-sea hydrothermal vents on the Mid-Atlantic Ridge, shrimps (*Rimicaris* aff. *exoculata*) swarm over the surface of black smoker chimney structures at the Kairei field. Video records show that the scaly-foot gastropod lives a sedentary life, alongside brachyuran crabs (*Austinograea* sp.), underneath shrimp swarms (see electronic supplementary material for video clips of observations described here). The "scaly-foot" gastropod inhabits the base of the chimney structures, where black hydrothermal fluids are emitted.

3.2. Nanostructural characteristics of the sclerites

Thin sections of the iron sulfide sclerties were examined by backscattered-electron imaging using a scanning electron microscope (SEM) equipped for energy dispersive X-ray spectroscopy (EDS). Sulfur was detected from the entire matrix of the sclerite by EDS analysis. Consistent with previous observations [1], typical sclerites contain three layers, as defined by the contents of iron sulfides. In order to identify the iron sulfide mineral phases and their spatial distribution, ultrathin sections produced by FIB milling were examined by transmission electron microscopy (TEM). A representative area containing the three layers identified by SEM was thinned to ~100 nm in thickness and observed by TEM (Fig. 2a). The outermost layer, with dark contrast, is mainly composed of iron sulfides and contains dense sub-micron iron sulfide inclusions, while the inner organic matrix contains two layers with

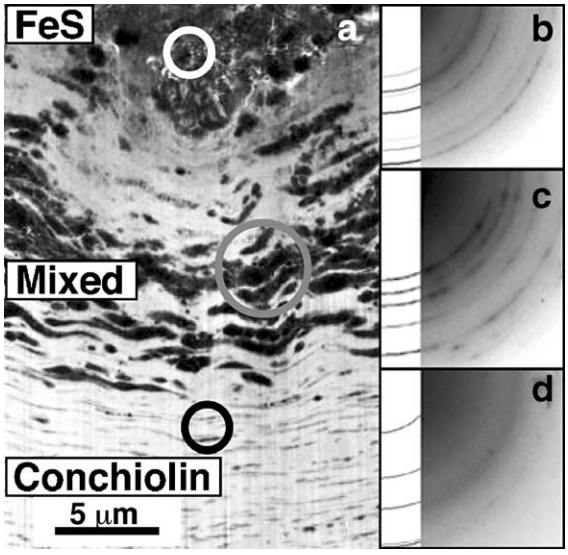

Fig. 2. Crystallographic characterization of iron sulfide phases in gastropod sclerites. (a) Transmission electron microscopy (TEM) image of the sclerite section after preparation by the FIB system. SAED patterns shown in (b)–(d) were obtained, respectively from regions in white, gray and black circles. (b) SAED patterns of greigite from the white circle region in the iron sulfide layer of the sclerite (right) and calculation (left). (c) SAED patterns of pyrite from the gray circle region in the mixed layer of the sclerite (right) and calculation (left). (d) SAED patterns of mackinawite from the black circle region in the conchiolin layer of the sclerite (right) and calculation (left).

different iron sulfide content and thin iron sulfide inclusions (Fig. 2a). Selected area electron diffraction (SAED) patterns obtained from the iron sulfide layer showed reflection rings with *d*-spacings of greigite (Fig. 2b). In contrast, SAED patterns from the mixed layer showed reflection rings with *d*-spacings identical to pyrite (Fig. 2c). Iron sulfides in the conchiolin layer have reflection rings and spots with *d*-spacings characteristic of mackinawite (Fig. 2d), although the rings are obscure due to the low concentration of the iron sulfide and the background from the organic matrix.

Observations of the iron sulfide layer by TEM revealed subparallel rod-shaped particles embedded in a lath of smaller fibrous material (Fig. 3a). Single crystal diffraction patterns identified the rod-shaped particles as greigite crystals elongated along the <110> axis (Fig. 3b). High-resolution (HR) TEM images (Fig. 3c) showed that the fibrous material consists mainly of mackinawite (FeS) with lattice fringes of ~0.5-nm spacing. Greigite crystals in the lath of fibrous material were identified by the fringes of 0.57-nm spacing attributed to d_{111} of greigite (Fig. 3c). The mackinawite crystals presumably have a foliated form, expanding parallel to the *a*–*b* plane. TEM obser-

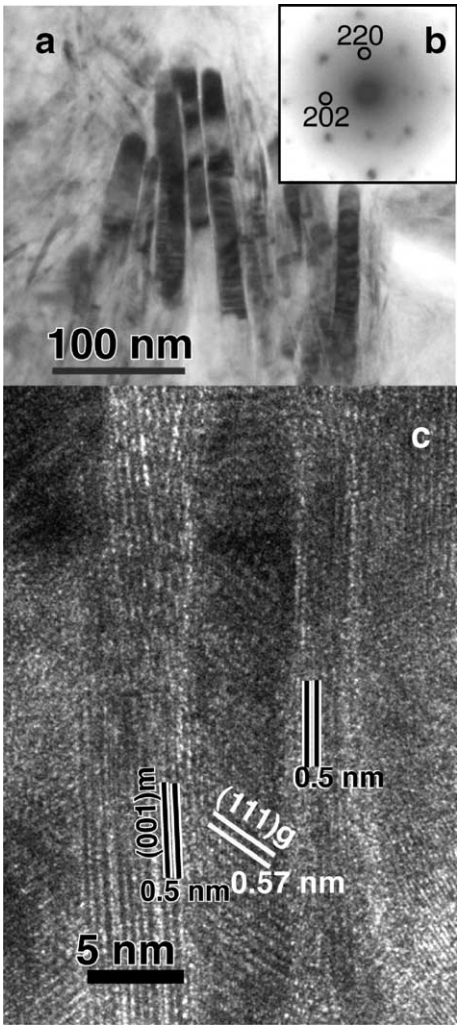

Fig. 3. High-resolution (HR) images of the iron sulfide layer. (a) TEM image of iron sulfide particles formed in the iron sulfide layer. Rod-shaped particles with darker contrast were observed. (b) SAED pattern from the single rod particle with *d*-spacings and systematic extinction identical to greigite. (c) HRTEM image of the interstitial iron sulfides showing the fringes of 0.5 nm spacing which correspond to (001) of mackinawite. The fringes of 0.57 nm spacing inside the rod-shaped particle correspond to {111} of greigite.

vations of the area in the mixed layer, from which SAED patterns characteristic of pyrite (Fig. 2c) were obtained, showed that each pyrite particle consists of clumps of small grains (Fig. 4a). Nevertheless, the pyrite particles diffract almost as a single crystal (Fig. 4b). HRTEM images showed that the grains are crystalline, with lattice fringes of ~0.38-nm spacing attributed to d_{110} of pyrite (Fig. 4c and d), and are as small as ~3 nm in size. The crystal orientation of the pyrite grains, as indicated by two-dimensional lattice fringes (marked with lines in Fig. 4c), was maintained throughout the particle. TEM observations of the mackinawite-bearing conchiolin layer showed that electron-dense dark regions are mainly composed of amorphous iron sulfide with minor mackinawite crystallites. The particle size of mackinawite ranges ~3–10 nm (Supplementary Fig. 1).

When aqueous iron(II) species reacts with hydrogen sulfide, amorphous iron monosulfide (FeS) forms initially for kinetic reasons [14] and then transforms into metastable mackinawite [15]. Mackinawite further transforms into greigite through a solid state reaction that involves changes in cubic closed packing of sulfur atoms by the loss of one-fourth of iron atoms and the oxidation of two thirds of the remaining iron [16]. As

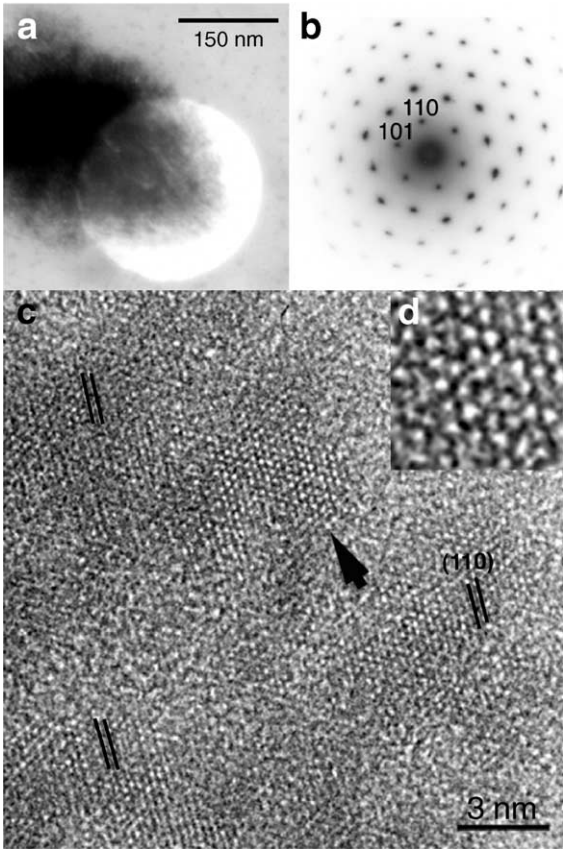

Fig. 4. High-resolution images of the mixed layer. (a) TEM image of a clump of iron sulfides formed in the mixed layer. From the bright circular region, the SAED pattern shown in (b) was obtained. (b) SAED pattern from the clump, showing the <111> pyrite projection. Note that the arced spots of high order reflections result from the misorientations. (c) HRTEM image of the clump of crystalline pyrite particles showing the fringe spacing of 0.38 nm which corresponds to {110} of pyrite and vacancies without lattice fringes. Although 110 of pyrite is an inhibited reflection, the corresponding fringes are visible due to the dynamical effect. (d) Enlarged image of the pyrite particles pointed by the arrow in (c).

mackinawite and greigite in the lath of fibrous material coexist in a similar size range (Fig. 3c), both might form in the processes described above.

The <110> elongation of the large rod-shaped greigite particles (Fig. 3a is different from the <100> elongation of greigite particles produced by magnetotactic bacteria [4]. Greigite particles from the magnetotactic bacteria, unlike the greigite rods, are believed to be elongated along their magnetocrystalline easy axes. Based on TEM observations, we determined the particle size and shape distribution of 30 relatively large, rod-shaped particles of greigite in the iron sulfide layer that were tilted into their zone axes. The average length, width and width/length ratio of these particles were 118 nm (S.D.=27 nm), 14 nm (S.D.=4 nm), and 0.12 (S.D.=0.3), respectively. Magnetotactic bacteria produce greigite particles in a size range comparable to the rod-shaped ones in the iron sulfide layer [4]. Greigite particles elongated along the <110> axis have previously been synthesized at acidic pH at 180 °C, but these particles were less than 50 nm in length [17]. It is therefore suggested that the rod-shaped greigite particles are unique, and may form through a previously unknown mechanism.

It has previously been reported that magnetotactic bacteria produce pyrite in addition to greigite [3,4]. However, this claim has been challenged because non-magnetic pyrite serves no function in magnetotaxis, and the pyrite might have formed under the harsh conditions of the TEM beam [4]. In the present study, we show that the mixed layer contains pyrite particles consisting of small grains in a size range previously unresolved (<5 nm). Laboratory and field studies have well established that pyrite formation also requires a precursor FeS phase [18,19]. Unlike the production of greigite, the transformation from amorphous FeS or mackinawite to pyrite involves the dissolution of the FeS phase(s) and the subsequent aqueous oxidation of S(-II) [19]. The extremely small pyrite grains are likely to nucleate from dissolved FeS complexes in the organic matrix, and the organic matrix may control the crystal growth by organizing the pyrite grains. The occurrence of the nanometer-sized pyrite grains was observed for the first time in the present study.

3.3. Magnetic studies of the sclerites

In contrast to organisms like chitons, which use magnetite as a hardening material in teeth, organisms that use magnetite for navigation generally optimize the size, shape, and arrangement of magnetic particles to maximize their magnetic moment [20]. To determine whether the sclerite material might be optimized for its magnetic properties, we conducted magnetic characterizations for the sclerites.

The zero-field low-temperature measurements (Fig. 5a) indicate no magnetic transition in the range of 2 K to 300 K, which is consistent with prior low-temperature measurements of greigite [21,22]. Our data did not show the 10 K remanence peak reported by Dekkers et al. [22]. The absence of transitions specifically excludes the presence of significant magnetite (which has a transition between 80 and 120 K), monoclinic pyrrhotite (which has a transition at 30–35 K), and hematite (which becomes a true antiferromagnet below 260 K). Measurements in a field of 5 mT (Fig. 5b) reveal transitions at 33 K and 250–270 K, perhaps indicating pyrrhotite and hematite, but these are minor components, with transitions causing changes of <2% in magnetization. The hematite may be an oxidation product formed after sample collection.

High-temperature measurements are consistent with a mixture of mackinawite, which is non-magnetic, and greigite (Fig. 6). The sample exhibits a doubling in magnetization between 100 °C and 180 °C, consistent with the transformation of mackinawite into greigite. A more gradual increase in magnetization occurs up to 275 °C. At higher temperatures, greigite is likely transformed into pyrrhotite. The magnetization decreases up to 350 °C, as the sample passes through the 320 °C Curie point of pyrrhotite. Upon cooling, the magnetization increases more gradually and less steeply than the decrease upon warming, also consistent with transformation of greigite to less strongly magnetic pyrrhotite. Strong rotational remanent magnetization (Fig. 7), acquired by rotating sclerites at 2–20 Hz in a 150 Hz

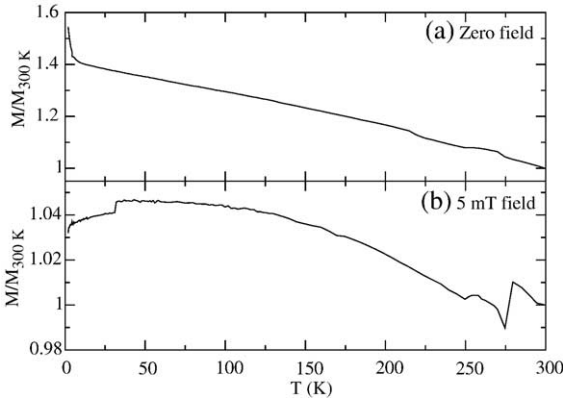

Fig. 5. Magnetization of a lateral sclerite plotted against temperature from 2 K to 300 K (a) in zero field and (b) in a 5 mT field. The minor transitions observed in the 5 mT field are likely due to pyrrhotite (at 33 K) and hematite (at 250–270 K).

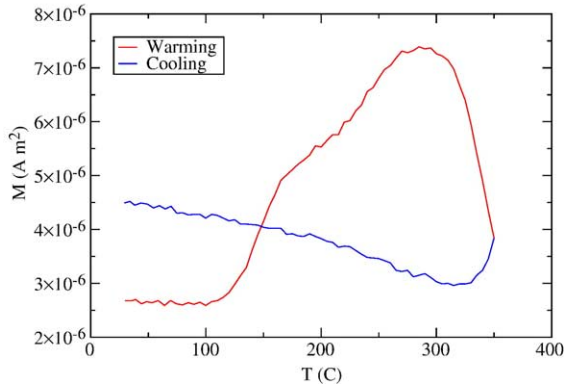

Fig. 6. Magnetization of a sclerite in 500 mT field upon heating to 350 °C and subsequent cooling to room temperature, plotted against temperature. The measurements are consistent with the transformation of mackinawite to greigite and the subsequent transformation of greigite to pyrrhotite.

alternating field, is also consistent with prior measurements of greigite [23].

Previous calculations of the single-domain field for greigite [24] suggest that the greigite rods observed by TEM should lie near the single-domain/superparamagnetic domain boundary, with a maximum coercivity of about 30 mT. Low-temperature measurements indicate a 45% loss of remanence upon warming from 2 K to 300 K, which is consistent with the presence of a significant superparamagnetic fraction (Fig. 3c). Room-temperature hysteresis parameters indicate a largely single-domain composition (Table 1). The incongruence between the low temperature and room temperature measurements likely reflects the stabilizing effect of interparticle interactions. Acquisition and demagnetization of isothermal remanent magnetization indicate a range of mean coercivities from 47 to 85

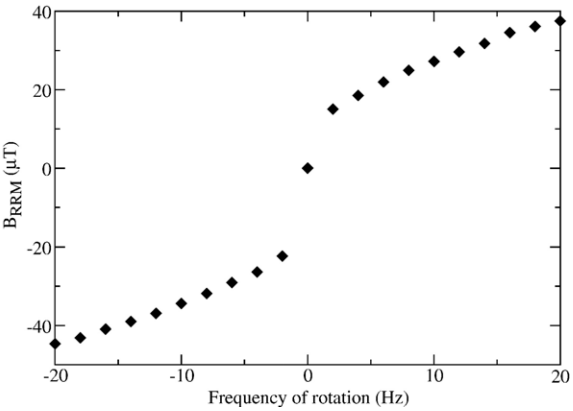

Fig. 7. Rotational remanent magnetization of a sclerite, expressed in terms of B_{eff}, the ARM biasing field necessary to produce an equivalent magnetization in the same alternating field, plotted against rotation rate.

Table 1
Room-temperature hysteresis properties determined by VSM

Sample	H_c (mT)	Mr/Ms
GastHy1	36.4	0.4481
GastLon1	32.02	0.5145
GastSq1	38.38	0.547
GastMlHy1	38.19	0.5428

mT (Table 2), which suggests that the calculations may have underestimated coercivity, or the gastropod samples may have occasional lattice defects.

Organisms that use magnetite for navigation generally produce single-domain grains, which optimizes the magnetic moment for the amount of Fe employed. Greigite has a broader single-domain field than magnetite, which increases the likelihood of a greigite-precipitating organism producing single-domain grains incidentally, without evolutionary optimization of grain dimensions. The presence of a significant superparamagnetic fraction also argues against optimized production of single-domain grains, though superparamagnetic grains might form as intermediates in the production of larger grains.

To further constrain the function of the magnetic sclerites, we measured the anhysteritic remanent magnetization (ARM) and also compared the natural remanent magnetization (NRM) with the isothermal remanent magnetization. ARM acquisition reflects the degree to which interparticle interaction dampens the sensitivity of particles to an external magnetic field. The magnetosome chains of magnetotactic bacteria, employed for navigation, are a good example of magnetic biomineral with minimal interparticle interactions, while chiton teeth, employed instead for hardening, have a high degree of interaction. The TEM observations suggest that significant interactions are likely, though the mackinawite crystals separating the greigite grains may provide enough separation to dampen interactions. ARM measurements (Fig. 8), however, reveal strong interparticle interactions; the ARM acquisition curve is nearly identical to that of the teeth of the chiton *Cyptochiton stelleri* [25]. Ferromagnetic resonance

Table 2
Coercivity of remanence and crossover values determined by acquisition and alternating field demagnetization of isothermal remanent magnetization

Sample	H_{cr} (mT)	R
SuzukiGrGastTail1	75.14	0.336
SuzukiGrGastTail3	84.66	0.31
GoffrediGrGast1	46.98	0.291

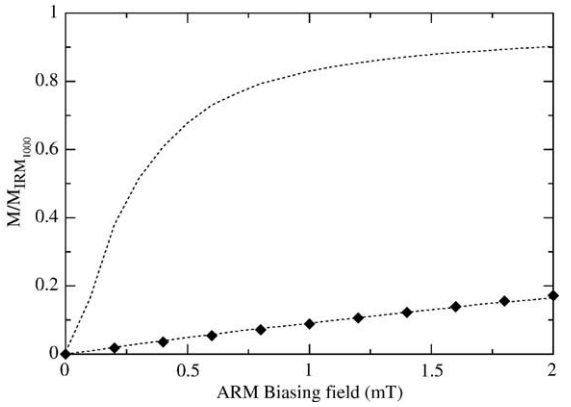

Fig. 8. Anhysteritic remanent magnetization acquired in an alternating field of 100 mT, expressed as a fraction of the isothermal remanent magnetization imparted by a 100 mT pulse. The upper dashed line is the magnetotactic bacterium standard, which exhibits little interaction effects. The lower dashed line, which largely coincides with the data, is the high-interaction chiton tooth standard.

spectroscopy (Fig. 9) [11] also indicates strong interaction effects, reflected by a high effective Landé g factor (g_{eff}=2.36–2.59).

The ratio of NRM to isothermal remanent magnetization (IRM) of the sclerites is extremely low, $10^{-3.4}$ (Fig. 10). This compares with a typical ratio for detrital remanent magnetizations of $\sim 10^{-3.0}$; chemical remanent magnetizations can range up to $\sim 10^{-2.0}$ [26]. This result is consistent with precipitation of the greigite crystals at a random distribution of orientations with respect to the Earth's field and is not consistent with use of the magnetic sclerites as a compass. Nevertheless, the greigite crystals of the sclerites do represent the second strongly magnetic mineral discovered in eukaryotes.

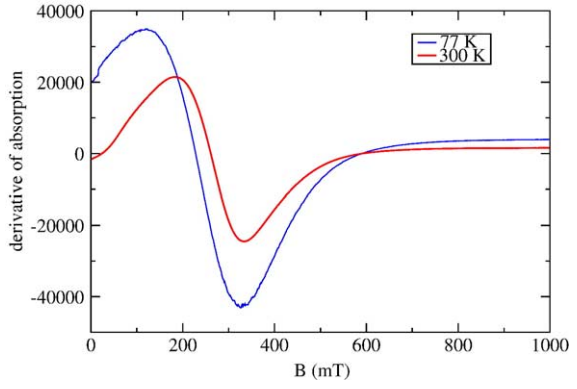

Fig. 9. Ferromagnetic resonance absorption of a tail sclerite. Shown is the first derivative of the X-band (9.4 GHz) power absorption with respect to the intensity of the applied DC field B, plotted as a function of B. The bold, red line records measurements taken at room temperature, while the thin, blue line records measurements taken at 77 K.

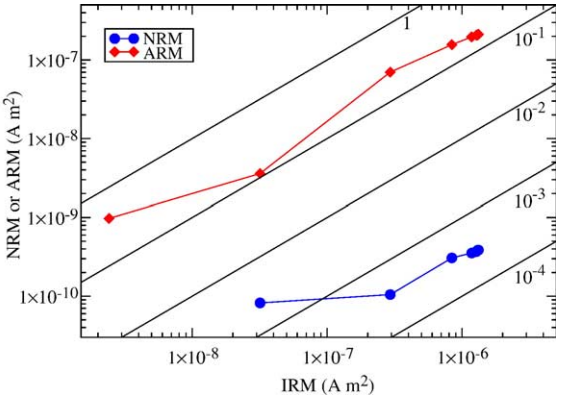

Fig. 10. AF demagnetization of NRM and ARM plotted against AF demagnetization of IRM. The ARM and NRM are of comparable hardness, both being slightly harder than IRM at low coercivities, but the NRM is much weaker in magnitude.

3.4. Mechanical properties

For quantitative comparison of the mechanical properties of the sclerites to those of biominerals used for predation or protection from predation, the hardness and elastic modulus (stiffness) of the iron sulfide and inner and mixed layers were determined by nanoidentation at the micrometer scale. The hardness and stiffness gradually decrease from the iron sulfide layer to the conchiolin layer (Table 3). The iron sulfide layer is harder and stiffer than human tooth enamel, which is made mostly of hydroxyapatite ($Ca_5(PO_4)_3(OH)$) [27]. The iron sulfide layer was also stiffer than molluscan shell nacre, which is mineralized with aragonite (Table 3) [28]. The mixed layer has superior mechanical properties in terms of its hardness and stiffness to those of dentin, which is the conchiolin of human teeth and is less densely mineralized with hydroxyapatite than enamel.

Table 3
Average hardness and elastic modulus values and their standard deviations of the iron sulfide sclerites, geological pyrite and other biomineralized materials

	Hardness (GPa)	Elastic modulus (GPa)
Sclerite		
Iron sulfide layer	9.97 ± 0.49[a]	113.11 ± 2.90
Mixed layer	2.16 ± 0.19	44.65 ± 1.54
Conchiolin layer	0.77 ± 0.03	13.51 ± 0.60
Geological pyrite	25.27 ± 0.28	253.27 ± 4.28
Enamel ([27])	4.78 ± 0.36	98.3 ± 5.90
Dentin ([27])	0.79 ± 0.04	24.8 ± 1.40
Nacre ([28])	ND[b]	73.0 ± 9.0

[a] Mean ± S.D. Nanoindention was conducted for three sclerites and geological pyrite grains.
[b] Not determined.

Although most minerals are stiff and brittle, the organic matrix itself is soft but tough. The combination of these opposite mechanical properties provides the mineral–organic matrix composite both rigidity and resistance against fracture [27]. The iron sulfide and conchiolin layers appear to be responsible respectively for the rigidity and toughness of the sclerites. The mixed layer, where nanometer-sized pyrite grains are embedded in the organic matrix, qualitatively seems both rigid and tough, though the toughness of the layer was not measured in the present study. It is suggested that, much like other biominerals evolutionarily optimized for their mechanical performance, the type, size, shape, density and location of the iron sulfide minerals are controlled by the gastropod. Similarly to the claim raised in [1], the main reason for the gastropod to harden its scleritome with iron sulfides may be to protect itself from predators such as co-occurring brachyuran crabs as documented in the video clips (see Electronic Supplementary Material).

3.5. Sulfur and iron isotopic analyses

To determine the source of sulfur for the gastropod and the iron sulfides in the sclerites, we analyzed the sulfur isotopic compositions (δ^{34}S) of soft body samples and of sclerites from several individual gastropods. As shown in Table 4, the δ^{34}S values of the iron sulfide sclerites (+2.7‰) are nearly identical to that of the soft body samples from the gastropods (+4.8‰) and from Bathymodiolid mussels in the same hydrothermal field (+3.4‰ to +5.6‰). The δ^{34}S values of the biological samples are also very close to those of sulfide chimneys (+4.4‰ to +7.1‰) and aqueous sulfide (+6.8‰ to +7.0‰), both of which are of hydrothermal origin [29,30], but clearly distinct from sulfate minerals (+19.1‰ to +20.2‰) from the relevant hydrothermal fluid and sulfate ions in seawater (~+20‰) [29]. Previously, it was suggested based on the detection of 16S rRNA gene sequences related to sulfate-reducing *Desulfobulbus* spp. from the sclerite surface that bacterial metabolites might be the sulfur source for the scleirtes [31]. As cultivated members of the genus *Desulfobulbus* fractionate sulfur isotopes during the production of hydrogen sulfide with fractionation factors of −5.5‰ to −6.8‰ for sulfate reduction [32] and −15.5‰ for disproportionation of elemental sulfur [33]. It seems unlikely that the majority of the sclerite sulfur originates from bacterial metabolites, unless the sulfate-reducing bacteria are sulfur limited. Thus, we interpret that the main sulfur source for the sclerites as well as the gastropod is most likely from hydrothermal fluids.

Table 4
Sulfur and iron isotopic compositions of the sclerite and softbody samples of the "scaly-foot" gastropods as well as vent fluids, sulfate and sulfide chimneys and the softbody samples of the Bathymodiolid mussels from the same field

Samples	δ^{34}S (‰)	δ^{56}Fe (‰)
The "scaly-foot" gastropod, sclerites	+2.7 ± 0.3[a]	−0.17 ± 0.21
The "scaly-foot" gastropod, softbody	+4.8 ± 0.5	−0.86 ± 0.22
Sulfide chimneys	ND[b]	+0.04 ± 0.16
Bathymodiolus marisindicus, softbody ([30])	+3.4 to +5.6	ND
Vent fluids ([29,30])	+6.8 to +7.0	ND
Sulfide chimneys ([30])	+4.4 to +7.1	ND
Sulfate minerals ([29])	+19.1 to +20.2	ND

Sulfur and iron isotopic compositions are reported respectively as δ^{34}S and δ^{56}Fe values (‰).
[a] Mean ± S.D. At least, duplicate measurements were conducted for each of triplicate samples. At least, two gastropod individuals were analyzed in the present study.
[b] Not determined.

It is becoming increasingly clear that iron isotopes are fractionated during natural processes, including transport, redox changes and assimilation by plants and animals [34,35]. To gain insight into the processes by which iron is supplied for iron sulfide mineralization, iron isotope ratios were measured for sclerites and soft body samples of gastropods and for sulfide chimneys from the same field. As shown in Table 4, the δ^{56}Fe values of the sclerites (−0.17‰) were almost indistinguishable from those of the sulfide chimneys (+0.04‰). In contrast, the δ^{56}Fe values of the soft body samples (−0.86‰) were depleted in ^{56}Fe, which is consistent with the fact that animals and plants preferentially assimilate lighter Fe isotopes [35]. From these iron isotopic data, it is inferred that, unless iron uptake is so efficient that it prevents expression of the metabolic kinetic isotope fractionation, iron in the sclerites is directly deposited from hydrothermal fluids without being assimilated by the gastropod.

3.6. Possible control on iron sulfide mineralization exerted by the gastropod

To incorporate minerals into a skeleton, several processes are involved: concentration of ions into a supersaturated solution, initiation and regulation of mineral growth, and positioning of the mineral bodies

in the organic matrix [8]. For greigite and pyrite to form, a precursor FeS phase and an oxidant are both necessary. The sulfur and iron isotopic data suggest that the availability of a precursor FeS phase to the sclerites might be determined by hydrothermal activity. If this is the case, the gastropod must be controlling the supply of oxidants for iron sulfide mineralization. For the formation of pyrite, several mechanisms were proposed:

A. "Ferrous iron loss pathway" [36]

$$2FeS(s) + 1/2H_2O + 3/4O_2 \rightarrow FeS_2(s) + FeOOH(s) \quad (2)$$

B. "Polysulfide pathway" [37,38]

$$FeS(s) + S^0(s) \rightarrow FeS_2(s) \qquad FeS(s) + S_n^{2-}(s) \rightarrow FeS_2(s) \quad (3)$$

C. "H_2S pathway" [19]

$$FeS(s) + H_2S \rightarrow FeS_2(s) + H_2 \quad (4)$$

In the case of pyrite formation, the oxidation of FeS by O_2 results in the formation of Fe(III) oxides (Eq. (2)), a fact which contradicts the absence of Fe(III) oxides in the mixed layer. It therefore seems likely that the gastropod controls iron sulfide mineralization by regulating the supply of reduced sulfur compounds (Eqs. (3) and (4)), a mechanism which is consistent with the small isotope fractionation exhibited during sulfur assimilation (Table 4 and [39]). It is not clear from the present study whether any organic molecules play roles in initiating and governing mineral formation, and how greigite and pyrite form separately in the sclerites.

3.7. Evolutionary implications for the iron sulfide scleritome

Lowenstam and Margulis [40] argued that the control of intracellular calcium ion concentrations, required for muscle contraction, secretion and cell adhesion, is a prerequisite for the development of calcareous skeletons. Similarly, animals that precipitate iron sulfide skeletal elements must likely regulate intracellular sulfide concentration. In the extreme environment of the hydrothermal vent, where the concentration of reduced sulfur compounds is high, regulation of sulfide concentration is also essential to avoid toxicity. In addition, it is likely that the gastropod nutritionally depends upon intracellular bacteria that synthesize organic matter from CO_2 by oxidizing reduced sulfur compounds [31]. Thus, it is plausible that the gastropod strictly regulates internal concentrations of these compounds not only to reduce their toxicity but also to control the growth of the bacterial endosymbiont. We speculate that such a system for the regulation of reduced sulfur compounds might have been involved in the evolution of the iron sulfide scleritome, which was later shaped and fine-tuned by natural selection by predators.

4. Conclusion

In the present study, we show for the first time the in-situ behavior of the gastropod and the nanostructure, magnetization and mechanical properties, sulfur and iron isotopic compositions of the iron sulfide scleritome. Our results support the inference that novel iron sulfide mineralization is directly mediated by the gastropod for protection against predation. To better understand the biomineralization of iron sulfides and the function of the scleritome, further investigations are needed. Of particular value would be studies of the long-term, in-situ behavior of the gastropod and other vent animals, the internal and external concentrations of reduced sulfur compounds, the metabolic activities of the bacterial endosymbiont, and scleritome development.

Acknowledgements

We thank the captains and crews of the R/V *Yokosuka* and the DSV *Shinkai 6500* operation group for their technical expertise. Comments from Stefan Bengtson, Anders Waren, Greg Druschel, Lev Neretin, Hidetoshi Urakawa, Jill Banfield, Mihaly Posfai, Rafal Dunin-Borkowski, Danielle Fortin, Shigeru Kuratani and Horst Felbeck significantly improved our manuscript. We acknowledge Shanna Goffredi for providing us sclerites for magnetic studies. The electron microscopy studies were mostly performed in the Electron Microbeam Analysis Facility of the Department of Earth and Planetary Science, the University of Tokyo. We thank Yozo Hamano of the University of Tokyo for use of the vibrating sample magnetometer for thermomagnetic analyses. REK was supported by a NSF Graduate Research Fellowship.

Appendix A. Supplementary data

Supplementary data associated with this article can be found, in the online version, at doi:10.1016/j.epsl.2005.11.029.

References

[1] A. Waren, S. Bengtson, S.K. Goffredi, C.L. Van Dover, A hot-vent gastropod with iron sulfide dermal sclerites, Science 302 (2003) 1007.

[2] R. Raiswell, R.A. Berner, Pyrite formation in euxinic and semi-euxinic sediments, Am. J. Sci. 286 (1985) 710–724.

[3] M. Farina, D.M.S. Esquivel, G.P. Henrique, H.G.P. Lins de Barros, Magnetic iron–sulphur crystals from a magnetotactic microorganism, Nature 343 (1990) 256–258.

[4] S. Mann, N.H.C. Sparks, R.B. Frankel, D.A. Bazylinski, H.W. Jannasch, Biomineralization of ferrimagnetic greigite (Fe_3S_4) and iron pyrite (FeS_2) in a magnetotactic bacterium, Nature 343 (1990) 258–261.

[5] H.A. Lowenstam, S. Weiner, On Biomineralization, Oxford University Press, Oxford, 1989, 324 pp.

[6] S. Bengtson, The cap-shaped Cambrian fossil Maikhanella and the relationship between coleoscleritophorans and molluscs, Lethaia 25 (1992) 401–420.

[7] S. Bengtson, V.V. Missarzhevsky, Coeloscleritophora—a major group of enigmatic Cambrian metazoans, in: M.E. Taylor (Ed.), Short Papers for the Second International Symposium on the Cambrian System, U.S. Geological Survey Open-File Report, vol. 81-743, 1981, pp. 9–21.

[8] S. Bengtson, The advent of animal skeletons, in: S. Bengtson (Ed.), Early Life on Earth, Nobel Symposium, vol. 84, Columbia U. P, New York, 1994, pp. 413–425.

[9] H.A. Lowenstam, Magnetite in denticle capping in recent chitons (*polyplacophora*), Geol. Soc. Am. Bull. 73 (1962) 435–438.

[10] J.L. Kirschvink, H.A. Lowenstam, Mineralization and magnetization of chiton teeth—paleomagnetic, sedimentologic, and biologic implications of organic magnetite, Earth Planet. Sci. Lett. 44 (1979) 193–204.

[11] B.P. Weiss, S.S. Kim, J.L. Kirschvink, R.E. Kopp, M. Sankaran, A. Kobayashi, A. Komeili, Ferromagnetic resonance and low temperature magnetic tests for biogenic magnetite, Earth Planet. Sci. Lett. 224 (2004) 73–89.

[12] W.C. Oliver, G.M. Pharr, An improved technique for determining hardness and elastic-modulus using load and displacement sensing indentation experiments, J. Mater. Res. 7 (1992) 1564–1583.

[13] F. Yanagisawa, H. Sakai, Thermal decomposition of bacterium sulfate-vanadium pentaoxide-sillica glass mixtures for preparation of sulfur isotope ratio measurements, Anal. Chem. 55 (1983) 985–987.

[14] D. Rickard, M.A.A. Schoonen, G.W. Luther III, Chemistry of iron sulphides in sedimentary environments, in: M.A. Vairamurthy, M.A.A. Schoonen (Eds.), Geochemical Transformations of Sedimentary Sulphur, ACS Symposium Series, vol. 61, 1995, pp. 168–193.

[15] A.R. Lennie, D.J. Vaughan, Spectroscopic studies of iron sulfide formation and phase relations at low temperatures, Geochem. Soc., Spec. Publ. 5 (1996) 117–131.

[16] M. Posfai, P.R. Buseck, D.A. Bazylinski, R.B. Frankel, Iron sulfides from magnetotactic bacteria: structure, composition, and phase transitions, Am. Mineral. 83 (1998) 1469–1481.

[17] S. Horiuchi, H. Wada, T. Moori, Morphology and imperfection of hydrothermally synthesized greigite (Fe_3S_4), J. Cryst. Growth 24/25 (1974) 624–626.

[18] L.G. Benning, R.T. Wilkin, H.L. Barnes, Reaction pathways in the Fe–S system below 100 degree C, Chem. Geol. 167 (2000) 25–51.

[19] D. Rickard, G.W. Luther III, Kinetics of pyrite formation by the H2S oxidation of iron (II) monosulfide in aqueous solutions between 25 and 125 °C: the mechanism, Geochim. Cosmochim. Acta 61 (1997) 135–147.

[20] M.M. Walker, T.E. Dennis, J.L. Kirschvink, The magnetic sense and its use in long-distance navigation by animals, Curr. Opin. Neurobiol. 12 (2002) 735–744.

[21] A.P. Roberts, Magnetic-properties of sedimentary greigite (Fe_3S_4), Earth Planet. Sci. Lett. 134 (1995) 227–236.

[22] M.J. Dekkers, H.F. Passier, M.A.A. Schoonen, Magnetic properties of hydrothermally synthesized greigite (Fe_3S_4): II. High- and low-temperature characteristics, Geophys. J. Int. 141 (2000) 809–819.

[23] I.F. Snowball, The detection of single-domain greigite (Fe_3S_4) using rotational remanent magnetization (RRM) and the effective gyro field (Bg): mineral magnetic and palaeomagnetic applications, Geophys. J. Int. 130 (1997) 704–716.

[24] J.C.D. Ricci, J.L. Kirschvink, Magnetic domain state and coercivity predictions for biogenic greigite (Fe_3s_4)—a comparison of theory with magnetosome observations, J. Geophys. Res.,-Solid Earth 97 (1992) 17309–17315.

[25] S. Cisowski, Interacting vs non-interacting single domain behavior in natural and synthetic samples, Phys. Earth Planet. Inter. 26 (1981) 56–62.

[26] M. Fuller, T. Kidane, J. Ali, AF demagnetization characteristics of NRM, compared with anhysteretic and saturation isothermal remanence: an aid in the interpretation of NRM, Phy. Chem. Earth 27 (2002) 1169–1177.

[27] H. Fong, M. Sarikaya, S.N. White, M.L. Snead, Nano-mechanical properties profiles across dentin–enamel junction of human incisor teeth, Mater. Sci. Eng. C-Biomim. Supramolecular Syst. 7 (2000) 119–128.

[28] A.P. Jackson, J.F.V. Vincent, R.M. Turner, The mechanical design of nacre, Proc. R. Soc. Lond., B 234 (1988) 415–440.

[29] T. Gamo, H. Chiba, T. Yamanaka, T. Okudaira, J. Hashimoto, S. Tsuchida, J. Ishibashi, S. Kataoka, U. Tsunogai, K. Okamura, Y. Sano, R. Shinjo, Chemical characteristics of newly discovered black smoker fluids and associated hydrothermal plumes at the Rodriguez Triple Junction, Central Indian Ridge, Earth Planet, Sci. Lett. 193 (2001) 371–379.

[30] T. Yamanaka, C. Mizota, Y. Fujiwara, H. Chiba, J. Hashimoto, T. Gamo, T. Okudaira, Sulphur-isotopic composition of the deep-sea mussel Bathymodiolus marisindicus from currently active hydrothermal vents in the Indian Ocean, J. Mar. Biol. Assoc. UK 83 (2003) 841–848.

[31] S.K. Goffredi, A. Waren, V.J. Orphan, C.L. Van Dover, R.C. Vrijenhoek, Novel forms of structural integration between microbes and a hydrothermal vent gastropod from the Indian Ocean, Appl. Environ. Microbiol. 70 (2004) 3082–3090.

[32] J. Detmers, V. Bruchert, K.S. Habicht, J. Kuever, Diversity of sulfur isotope fractionations by sulfate-reducing prokaryotes, Appl. Environ. Microbiol. 67 (2001) 888–894.

[33] D.E. Canfield, B. Thamdrup, S. Fleischer, Isotope fractionation and sulfur metabolism by pure and enrichment cultures of elemental sulfur-disproportionating bacteria, Limnol. Oceanogr. 43 (1998) 253–264.

[34] A.D. Anbar, Iron stable isotopes: beyond biosignatures, Earth Planet. Sci. Lett. 217 (2004) 223–236.

[35] T. Walczyk, F. von Blanckenburg, Natural iron isotope variations in human blood, Science 295 (2002) 265–266.

[36] R.T. Wilkin, H.L. Barnes, Pyrite formation by reactions of iron monosulfides with dissolved inorganic and organic sulfur species, Geochim. Cosmochim. Acta 60 (1996) 4167–4179.
[37] R.A. Berner, Iron sulfides formed from aqueous solution at low temperatures and atomospheric pressure, J. Geol. 72 (1964) 293–306.
[38] W. Luther III, Pyrite synthesis via polysulphide compounds, Geochim. Cosmochim. Acta 55 (1991) 2839–2849.
[39] D.E. Canfield, Biogeochemistry of sulfur isotopes, Mineralogical Society of America Reviews in Mineralogy and Geochemistry, vol. 43, 2001, pp. 607–636.
[40] H.A. Lowenstam, L. Margulis, Evolutionary prerequisites for early phanerozoic calcreous skeletons, BioSystems 12 (1980) 27–41.